



OPEN

SUBJECT AREAS:  
CARBON NANOTUBES  
AND FULLERENES  
POROUS MATERIALSReceived  
12 July 2013Accepted  
25 September 2013Published  
22 October 2013Correspondence and  
requests for materials  
should be addressed to  
Y.H.L. (leeyoung@  
skku.edu)

# TLM-PSD model for optimization of energy and power density of vertically aligned carbon nanotube supercapacitor

Arunabha Ghosh<sup>1,2</sup>, Viet Thong Le<sup>1,2</sup>, Jung Jun Bae<sup>1,2</sup> & Young Hee Lee<sup>1,2</sup><sup>1</sup>IBS Center for Integrated Nanostructure Physics, Institute for Basic Science (IBS), Sungkyunkwan University, Suwon 440-746, Republic of Korea, <sup>2</sup>Sungkyunkwan Advanced Institute of Nanotechnology, Department of Energy Science, Department of Physics, Sungkyunkwan University, Suwon 440-746, Republic of Korea.

Electrochemical capacitors with fast charging-discharging rates are very promising for hybrid electric vehicle industries including portable electronics. Complicated pore structures have been implemented in active materials to increase energy storage capacity, which often leads to degrade dynamic response of ions. In order to understand this trade-off phenomenon, we report a theoretical model based on transmission line model which is further combined with pore size distribution function. The model successfully explained how pores length, and pore radius of active materials and electrolyte conductivity can affect capacitance and dynamic performance of different capacitors. The powerfulness of the model was confirmed by comparing with experimental results of a micro-supercapacitor consisted of vertically aligned multiwalled carbon nanotubes (v-MWCNTs), which revealed a linear current increase up to 600 Vs<sup>-1</sup> scan rate demonstrating an ultrafast dynamic behavior, superior to randomly entangled singlewalled carbon nanotube device, which is clearly explained by the theoretical model.

Supercapacitor, an electrochemical capacitor with high surface area, shows excellent power density and has attracted much attention recently due to the demand of fast charging for technological relevance to portable electronics. Yet, supercapacitor suffers from poor energy density compared to its counterpart of battery, limiting the applications. Power density and energy density are trade-off quantities which require an optimization. Electrochemical properties of supercapacitor can be greatly influenced by several parameters; surface area, conductivity, porosity, and types of electrode materials<sup>1-3</sup>. High surface area usually increases electric double layer capacitance (EDLC)<sup>4</sup>. High conductivity leads to high power density and long cycle life<sup>5</sup>. Presence of abundant micropores increases total surface area and energy density, as also shown by recent developments based on several metal-organic frameworks or porous coordination polymers<sup>6-9</sup>, while absence of mesopores limits ion diffusion, degrading power density<sup>10</sup>. Introduction of metal oxides increases pseudocapacitance but degrades cyclability<sup>11</sup>. Increasing porosity degrades conductivity<sup>10</sup>. Loading large amount of materials in electrode is necessary for high energy density but increases total diffusion length, again leaving poor power density<sup>12</sup>. Therefore, in order to understand a design rule of supercapacitor electrode, a systematic strategy of designing mesoporous structures with high surface area and combination of micropores and mesopores in addition to the choice of materials need to be constructed.

There have been several reports on constructing micro-supercapacitors due to the technological demands for energy storage in microelectromechanical system (MEMS)<sup>13-25</sup>. Micro-supercapacitors based on polyaniline and polypyrrole have exhibited promising volumetric capacitance but suffered from low rate capability, inferior frequency response, and poor cyclic stability<sup>13-17</sup>. Different carbon materials such as activated carbon, carbide-derived carbon, and reduced graphene oxides have been tried as active materials of micro-electrodes but their capacitive performance could not be retained particularly at high scan rate<sup>18-20</sup>. Relaxation time constant is a measure of time required to discharge 50% of total stored energy<sup>21</sup>. The device operates faster at a smaller value of relaxation time constant. Recent reports showed improved relaxation time constant of 3.4, 26, and 19 ms for micro-supercapacitors with graphene-CNT<sup>21</sup>, onion-like carbon<sup>22</sup>, and graphene-oxide<sup>23</sup>, respectively. Even faster devices have been reported with extremely low value of relaxation time constant of 0.2 and 0.238 ms using oriented graphene<sup>24</sup> and reduced graphene oxide<sup>25</sup> but their obtained capacitances and energy densities per unit area were very low, which is a consequence of low mass density of the electrodes. These results again indicate that



a systematic theoretical study is required as well as more elaborated experimental studies to obtain the optimized mesoporous structures for supercapacitors.

The main purpose of the paper is to find a strategy to design the best mesoporous material for supercapacitors by constructing a theoretical model and performing the related experiments. This will enable us to understand how the nature of porosity of materials influences the energy density and the rate capability (i.e., relaxation time constant) which is further related to the power density. Here we established a theoretical scheme to model mesoporous structure where capacitance can be obtained from theoretical calculations based on frequency distribution of porous electrode using Levie's transmission line model (TLM)<sup>26–28</sup>. Information of pore size distribution (PSD) combined with transmission line model (TLM-PSD) can be used to simulate frequency response of entire electrode<sup>29</sup>. Using this model, we have done a systematic study to investigate the dependence of relaxation time constant on several parameters, such as pore length and diameter, density of active material, electrode thickness, and electrolyte conductivity.

In order to validate our model, we have done a series of experiments by fabricating a MEMS supercapacitor with vertically aligned multiwalled carbon nanotubes (v-MWCNTs), which is suitable to check the validity of the model by providing regular porosity with controllable pore radius and pore length. We found satisfactory match between experiments and model calculations, assuring that optimization of mesoporous structures are possible within theoretical model. In addition, we have carried out a proof of concept experiment using micro-devices based on randomly entangled single walled carbon nanotubes (re-SWCNTs). This comparative study exhibited the superiority of vertically aligned structure over entangled planar CNTs in terms of rate capability.

## Results

The interstitial pores of v-MWCNTs can be considered as a well aligned mesoporous structure, whose pore diameter is dependent on the density of v-MWCNTs<sup>30</sup>. Figure 1a shows a schematic of the MEMS device, fabricated on a SiO<sub>2</sub> wafer. Active materials are present on top of the supporting electrodes, which are connected to the contact electrodes. The micro-device has two parallel inter-digital electrodes. Each of these two electrodes is made of nine finger-like structures which are connected to each other. Figure 1b shows a schematic of a cylindrically shaped pore in purple-green color, in the interstitial space of v-MWCNTs. Scanning electron microscope (SEM) image of a micro-supercapacitor device made of v-MWCNTs is shown in Fig. 1c–1e with magnified images of inter-digital electrode. Figure 1e measures height of v-MWCNTs of 55  $\mu\text{m}$ .

The MEMS structure with v-MWCNTs can be considered as parallel arrays of similar cylindrical pores, as shown in Fig. 1b. Therefore, a mathematical expression, which represents the total impedance of the above mentioned arrays of cylindrical pores, can be used to derive the complex capacitance. In complex capacitance analysis, the electrode of supercapacitor is considered as a whole capacitor. From impedance analysis, the frequency distribution of real and imaginary part of the capacitance and the relaxation time constant of active material can be derived<sup>31</sup>.

Total impedance of the electrode is the equivalent impedance of electrical circuit made of all the cylindrical pores in parallel (see Fig. S1). When electrochemical activity of the porous electrode is limited to pure electric double layer interaction, i.e., no faradaic reaction with negligible sluggish process (for instance, surface reconstruction), the impedance of the porous structure is governed by the geometry of such pores, and can be represented by the following equation<sup>29</sup>,

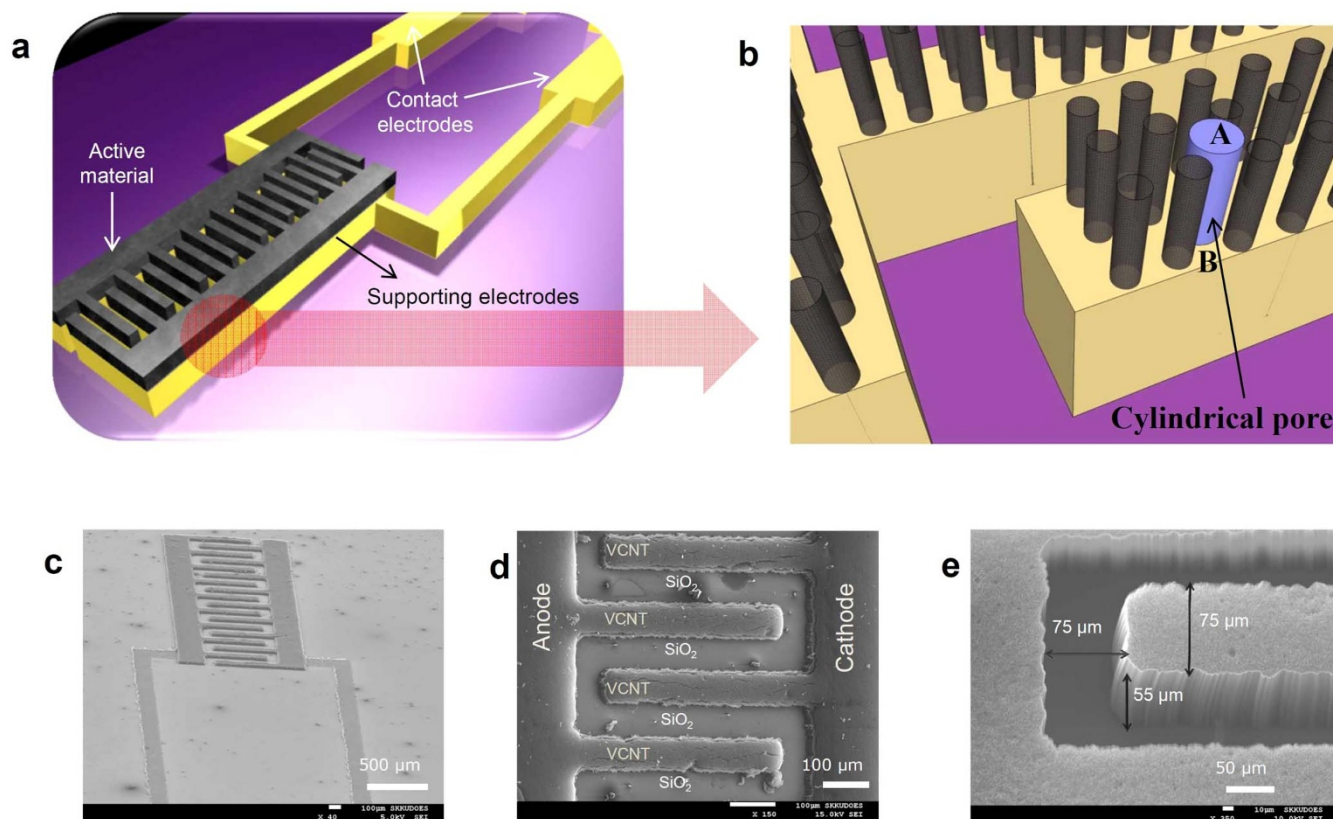


**Figure 1** | (a) Schematic of micro-device, (b) cylindrical pore formed in the interstitial space of v-MWCNTs, (c) SEM image of micro-device, (d) magnified image of the micro-device with 15  $\mu\text{m}$  long CNTs, and (e) SEM image measures a height 55  $\mu\text{m}$ .



$$Z_p^* = \left[ \frac{\sinh(1/\alpha) - \sin(1/\alpha)}{\cosh(1/\alpha) - \cos(1/\alpha)} - j \frac{\sinh(1/\alpha) + \sin(1/\alpha)}{\cosh(1/\alpha) - \cos(1/\alpha)} \right]; \quad (1)$$

with,  $Z_p^* = \frac{Z_p}{R_O}$ ,  $R_O = \frac{1}{\kappa} \frac{l_p}{\pi r^2}$ ,  $\alpha = \frac{\lambda}{l_p}$ ,  $\lambda = \frac{1}{2} \sqrt{\frac{\kappa r}{C_d^* \omega}}$ ; where  $Z_p$  is the impedance of a pore (ohm);  $Z_p^*$  is the reduced impedance [impedance normalized by  $R_O$ ;  $R_O$  is the electrolyte resistance in a pore (ohm)];  $\alpha$  is the penetrability;  $\lambda$  is the penetration depth (cm);  $l_p$  and  $r$  are the length (cm) and radius of a pore (cm);  $\kappa$  and  $C_d^*$  are the electrolyte conductivity ( $\text{ohm}^{-1} \text{cm}^{-1}$ ) and the effective electric double layer capacitance at the interface between electrolytes and electrodes ( $\text{F cm}^{-2}$ ), respectively and  $\omega$  is the angular frequency (rad/s). Here, Eq. (1) simulates the reduced impedance of a pore. When all such pores are considered along with their distribution function,  $f(\vec{S}, r)$  within the electrode material, total impedance of the electrode can be obtained by following volume integral (throughout entire active material),

$$\frac{1}{Z} = \int_v \frac{1}{Z_p^*(\vec{S}, r) R_O(\vec{S}, r)} [f(\vec{S}, r)] dv, \quad (2)$$

where,  $Z_p^*(\vec{S}, r)$  is the reduced impedance of a pore with radius  $r$  and located at a spatial position  $\vec{S}$ , and  $R_O(\vec{S}, r)$  represents electrolyte resistance in that pore.  $f(\vec{S}, r)$  represents PSD of active material. Equation (2) represents TLM-PSD model, taking account of PSD along with TLM of the micro-electrode. Here PSD is uniform for regularly spaced vertical CNT array, and  $f(\vec{S}, r)$  becomes independent of  $\vec{S}$ , and is a delta function of radius of pore ( $r$ ) for a given v-MWCNT density and equals to unity.  $Z_p^*(\vec{S}, r)$  and  $R_O(\vec{S}, r)$  are also independent of  $\vec{S}$ , as the v-MWCNTs arrays are regularly spaced regardless of their position. Therefore, the total impedance of the

electrode can be reduced to the following equation by summing parallel pores;

$$\frac{1}{Z} = \sum_{i=1}^n \frac{1}{Z_p^* R_O}, \quad (3)$$

where  $n$  is the total number of pores.

From total impedance of the micro-device, the imaginary part of the complex capacitance can be obtained from the following equation<sup>32</sup>;

$$C_{imag} = \frac{Z_{real}(\omega)}{\omega |Z(\omega)|^2}, \quad (4)$$

where,  $C(\omega) = C_{real}(\omega) - jC_{imag}(\omega)$ ; and  $Z(\omega) = Z_{real}(\omega) + jZ_{imag}(\omega)$ . Here,  $C(\omega)$  and  $Z(\omega)$  are the total effective capacitance and impedance of the micro-electrode.  $C_{real}(\omega)$ ,  $Z_{real}(\omega)$  are the respective real part, and  $C_{imag}(\omega)$ ,  $Z_{imag}(\omega)$  are the imaginary part of the effective capacitance and impedance of the microelectrode.

Equation (4) was used to fit experimentally obtained results for frequency distribution of imaginary part of capacitance with a frequency range from 1 Hz to 100 kHz from electrochemical impedance spectra (EIS), which is shown in Fig. 2a. Experimental data (shown by symbols) was obtained for 10  $\mu\text{m}$  high v-MWCNTs in 1 M  $\text{Li}_2\text{SO}_4$  electrolyte. The continuous line represents simulated results. For the above fitting,  $\kappa = 0.048 \text{ ohm}^{-1} \text{cm}^{-1}$  for  $\text{Li}_2\text{SO}_4$  electrolyte<sup>33</sup> and effective differential capacitance  $C_d^* = C_d \times (r_{\text{CNT}}/r)$ ,  $C_d = 50 \mu\text{F cm}^{-2}$  as EDLC capacitance<sup>34</sup>, were used. Differential capacitance  $C_d$  is multiplied by a structure factor ( $r_{\text{CNT}}/r$ ) to take account of effective contribution of the surface area of CNT, where  $r_{\text{CNT}}$  is the radius of individual CNTs. Pore length,  $l_p$  was taken equal to the height of CNTs (10  $\mu\text{m}$ ) and pore diameter was determined by the separation distance between two adjacent CNTs (See S.I. Fig. S2). Using the above mentioned parameters we

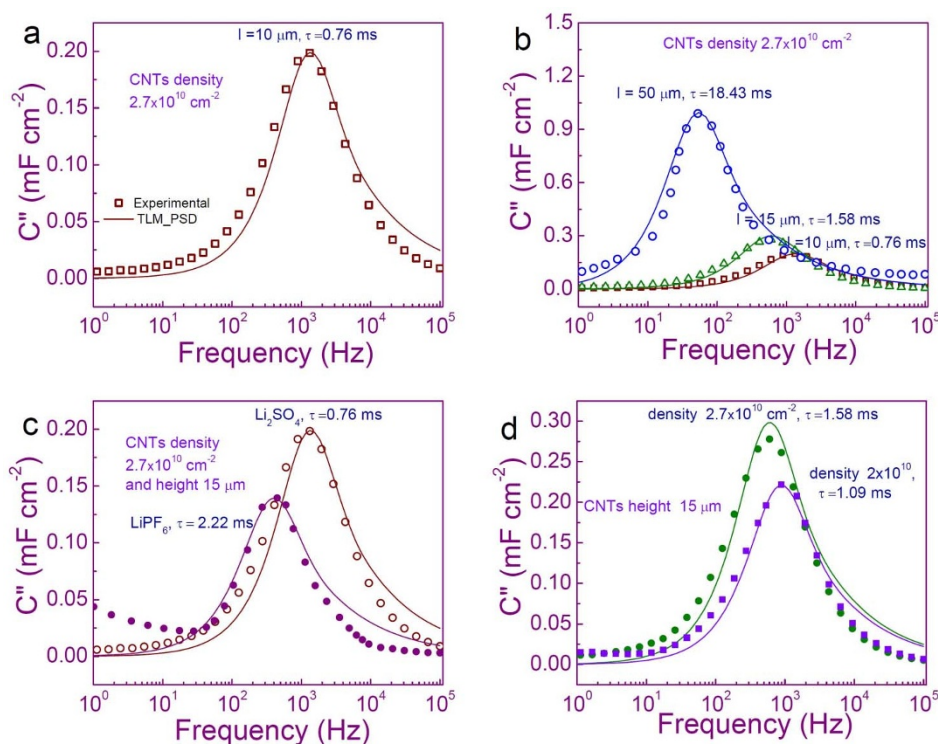


**Figure 2** | Fitting measured imaginary capacitance with theoretical model for (a) 10  $\mu\text{m}$  long v-MWCNT electrode with a time constant of 0.76 ms for a CNT density of  $2.7 \times 10^{10} \text{ cm}^{-2}$  and (b) the corresponding plot for different heights (10, 15, and 50  $\mu\text{m}$ ) of v-MWCNTs. (c) The corresponding curves obtained for  $\text{Li}_2\text{SO}_4$  and  $\text{LiPF}_6$  electrolytes for 10  $\mu\text{m}$  long v-MWCNTs and (d) curves obtained for two different CNT densities ( $2.7 \times 10^{10} \text{ cm}^{-2}$  and  $2.0 \times 10^{10} \text{ cm}^{-2}$ ) for a fixed 15  $\mu\text{m}$  height in  $\text{Li}_2\text{SO}_4$  electrolyte.





found a reasonably good fitting of our result for a v-MWCNT density of  $2.7 \times 10^{10} \text{ cm}^{-2}$  (Fig. 2a). The total number of pores will be approximately equal to the number of CNT density, as there is a pore between every two CNTs (See S. I. Fig. S2). Figure 2a shows the maximum imaginary part of capacitance at a characteristic frequency ( $f_0$ ) of 1322 Hz, which represents a relaxation time constant ( $\tau = 1/f_0$ ) of 0.76 ms. The theoretical fitting also represents well the characteristic peak with a slight deviation at lower and higher frequency regions. The discrepancy at the lower frequency region is attributed to the possible contribution from the existence of micropores and redox reaction due to the presence of defects at the CNT surface, whereas at higher frequency region, some CNTs are overlapped to change the effective surface area of CNTs. The presence of these defects was further confirmed by the obtained Raman spectra of v-MWCNTs (See Fig. S3). Micropores were excluded in our model that the uniform interstitial mesopores are present only.

The validity of our model was further confirmed by fitting another two sets of experimental data which were obtained from CNTs with two different heights of 15 and 55  $\mu\text{m}$  (Fig. 2b). Simulation was carried out by keeping all other parameters unchanged (S.I. Table - S1), except the variation in pore lengths which were taken as 15 and 48.5  $\mu\text{m}$  in eqn. (1). Although a slight variance for high pore height of 55  $\mu\text{m}$  was observed in the simulation, the data were fitted well in most frequency ranges, proving the validity of our model. It is noted that with increasing height of v-MWCNTs, the peak capacitance increases and at the same time the peak positions were shifted to lower frequency region (See S.I. Table S1). With increasing the height of nanotubes, the increment in complex capacitance is obvious from the increased surface area of v-MWCNTs per unit electrode area. On the other hand, a gradual increment of relaxation time constants can be explained by the increased diffusion path length for longer CNTs, in which this effect was mathematically embedded in our model through eqn. (1) ( $R_0 = \frac{1}{\kappa} \frac{l_p}{\pi r^2}$ ).

Figure 2c shows the comparison of the micro-devices for different types of electrolytes. EIS spectra were recorded for a device with 10  $\mu\text{m}$  high v-MWCNTs in aqueous electrolyte of  $\text{Li}_2\text{SO}_4$  and non-aqueous electrolyte of 1.15 M  $\text{LiPF}_6$  in Ethylene carbonate/Diethyl carbonate (EC/DEC) solvent [EC/DEC = 3/7 (v/v)]. The device exhibited a poor rate capability in  $\text{LiPF}_6$  with high value of relaxation time constant of 2.22 ms compared to 0.76 ms in  $\text{Li}_2\text{SO}_4$ , which is reflected from the ionic conductivity difference between  $\text{LiPF}_6$  ( $0.010 \text{ ohm}^{-1} \text{ cm}^{-1}$ )<sup>35</sup> and  $\text{Li}_2\text{SO}_4$  ( $0.048 \text{ ohm}^{-1} \text{ cm}^{-1}$ )<sup>33</sup>. The magnitude of capacitance was also lower in  $\text{LiPF}_6$  ( $135.6 \mu\text{F cm}^{-2}$ ) than in  $\text{Li}_2\text{SO}_4$  ( $198.4 \mu\text{F cm}^{-2}$ ). Effect of the conductivity change was again confirmed by fitting experimentally obtained results with simulation data (continuous lines in Fig. 2c), which was directly obtained from eqn. (1) by using known experimental conductivities of  $\text{LiPF}_6$  and  $\text{Li}_2\text{SO}_4$ . In order to fit the experimental results in  $\text{Li}_2\text{SO}_4$ , we used a differential capacitance of  $50 \mu\text{F cm}^{-2}$  (ref. 34), which is typically obtained for electric double layer capacitor with planar metal electrodes<sup>36</sup>. For non-aqueous electrolyte ( $\text{LiPF}_6$ ), the differential capacitance was extracted from fitting as  $35 \mu\text{F cm}^{-2}$ . The lower value of the extracted  $C_d$  in the case of  $\text{LiPF}_6$ , can possibly be explained by the lower dielectric constant of non-aqueous electrolytes and larger ion size of  $\text{PF}_6^-$  compared to that of  $\text{SO}_4^{2-}$  in aqueous electrolyte<sup>37–40</sup>. From the model we note easily that the rate capability of the micro-device is affected by the increased CNT height and the reduced conductivity of electrolyte. Density of the CNT array is another key parameter which can control the rate capability of the device. Figure 2d shows the effect of the CNT density on the rate capability of the device. EIS spectra were obtained and analyzed for a micro-device with less CNT density ( $2.0 \times 10^{10} \text{ cm}^{-2}$ ) in  $\text{Li}_2\text{SO}_4$ , and was compared with previously mentioned micro-device with a CNT density of  $2.7 \times 10^{10} \text{ cm}^{-2}$ , while keeping CNT height of 15  $\mu\text{m}$ . Lower density of the device was obtained by

changing thickness of Fe catalyst layer. With increasing thickness of Fe catalyst layer, the number density of Fe nanoparticles was reduced, hence giving rise to lower CNT density<sup>41</sup>. In our micro-device, it was extremely difficult to quantify the exact number of CNT density. Nevertheless, the obtained experimental results were well fitted to a model with a CNT density of  $2.0 \times 10^{10} \text{ cm}^{-2}$ , while all other parameters kept unchanged. Lower density of CNTs resulted in the upshift of the peak position of capacitance and relaxation time constant to 1.03 ms from 1.58 ms, and at the same time the capacitance value was reduced to  $221 \mu\text{F cm}^{-2}$  from  $298 \mu\text{F cm}^{-2}$ , which was a direct consequence of reduction of the total active mass of CNTs on the electrode. The lower rate capability can be explained by slower ion diffusion due to the increased pore resistance, which is a consequence of the reduced pore radius for denser CNT arrays (eqn. (1)).

We have considered so far vertically aligned pores in the interstitial region of v-MWCNT arrays. These pores are parallel to each other and therefore vertically downward motion of the ions inside the pores is taken account only. On the other hand, in a planar MEMS supercapacitor structure, positive and negative electrodes are positioned in side by side configuration, unlike vertical electrodes configuration in sandwiched supercapacitor structure. Therefore, electric field lines due to applied DC potential across the anode and cathode are applied along horizontal direction, from positive to negative electrodes, which will eventually produce ionic motion in side direction (See Fig. S4). The ions are thus expected to flow through interstitial region of v-MWCNTs along horizontal direction (See the supporting information, Fig. S5a–c). As a result, there is a possibility to have an effective pore formation along horizontal direction in addition to interstitial pore formation along vertical direction. We have therefore considered another model with pores along horizontal direction, as shown in Fig. S5a. Nevertheless, we observed that there is no change in the relaxation time constant (or characteristic frequencies) with increasing v-MWCNT height (Fig. S5). This was inconsistent with experimental observations in which the capacitance and relaxation time altered with CNT height. Therefore, the possibility of contribution from the side wall diffusion, although the field is applied along the side direction, could be excluded.

To confirm the validity of our observations, we have solved Laplace equation numerically to extract electric field line information by simulating a finite element method (AC/DC module, Comsol) (see supporting information, S2). With two different conductivities of CNTs contacted with Al, The field line reveals some degree of side component (perpendicular to CNT walls) between adjacent electrodes, as shown in Fig. 3a. What is intriguing is that at the top of the CNT surface, the field lines point toward the top direction due to strong field enhancement effect at the sharp CNT tip and even at the side wall, parallel component to the CNT walls still appears. More importantly, the field lines are almost parallel to the CNT walls inside CNT electrode. This is due to the charge accumulation at interface between Al and CNT bottom with different conductivities. On the other hand, the field line distribution is slightly different when the same conductivities are used, as shown in Fig. 3b. The field line does not exist inside metals due to equipotential surfaces. The field lines are more preferentially perpendicular at the top surface, while at the side walls, they are perpendicular to the side walls. The former model in Fig. 3a is more suitable for our experimental situation and theoretical model. Even though ions move in sideways direction in between two planar electrodes, eventually ions move in vertical direction inside v-MWCNT arrays. Therefore, we believe that the interstitial pores formed along the CNTs are more appropriate, supporting our modeling.

A more systematic model investigation was done for the effect of the CNT density on the relaxation time constant. As the CNT density varied from  $1.0 \times 10^{10}$  to  $4.0 \times 10^{10} \text{ cm}^{-2}$ , the relaxation time constant increased linearly from 0.48 to 2.81 ms and correspondingly

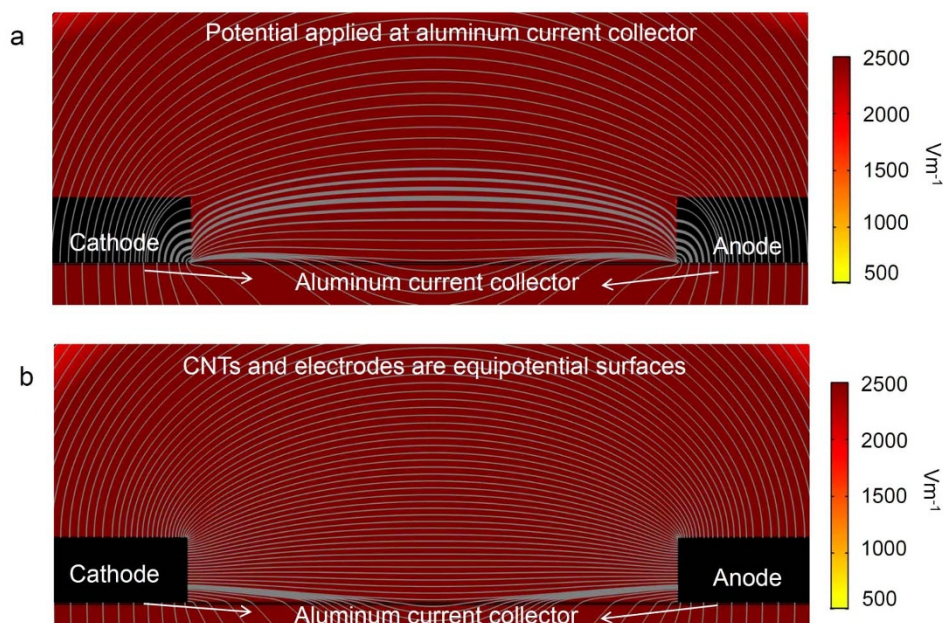


**Figure 3** | Electric field line distributions in between anode and cathode of micro-supercapacitor device (2D side view) in two different configurations. (a) The potential is applied only at Al current collector. We have considered two media with conductivities  $3 \times 10^5 \text{ ohm}^{-1} \text{ cm}^{-1}$  ( $\nu$ -MWCNTs) and  $3.53 \times 10^5 \text{ ohm}^{-1} \text{ cm}^{-1}$  (Al), connected in series. (b)  $\nu$ -MWCNTs and Al current collector are regarded as the same material with a conductivity of  $3.53 \times 10^5 \text{ ohm}^{-1} \text{ cm}^{-1}$ .

the capacitance also increased almost linearly from 110 to 440  $\mu\text{F cm}^{-2}$  (Fig. 4a–b). Similar systematic study was carried out for different heights of CNTs (Fig. 4c–d). As the CNT length varied from 10 to 50  $\mu\text{m}$ , the relaxation time constant and capacitance increased almost quadratically as well.

For a proof of concept of the model, we have carried out further a series of experiments by constructing a random porous structure, i.e.,

randomly entangled singlewalled CNTs (re-SWCNTs). Dichloroethane (DCE)-dispersed SWCNTs were sprayed on Au current collector of the micro-device. Figure 5a shows the schematic of the re-SWCNTs based micro-device. Random distribution of the active material can be easily observed from the top view of the schematic. The SEM image of the entire micro-device is shown in Fig. 5b–d with the magnified tilt image of re-SWCNT films and  $\text{SiO}_2$  regions in the

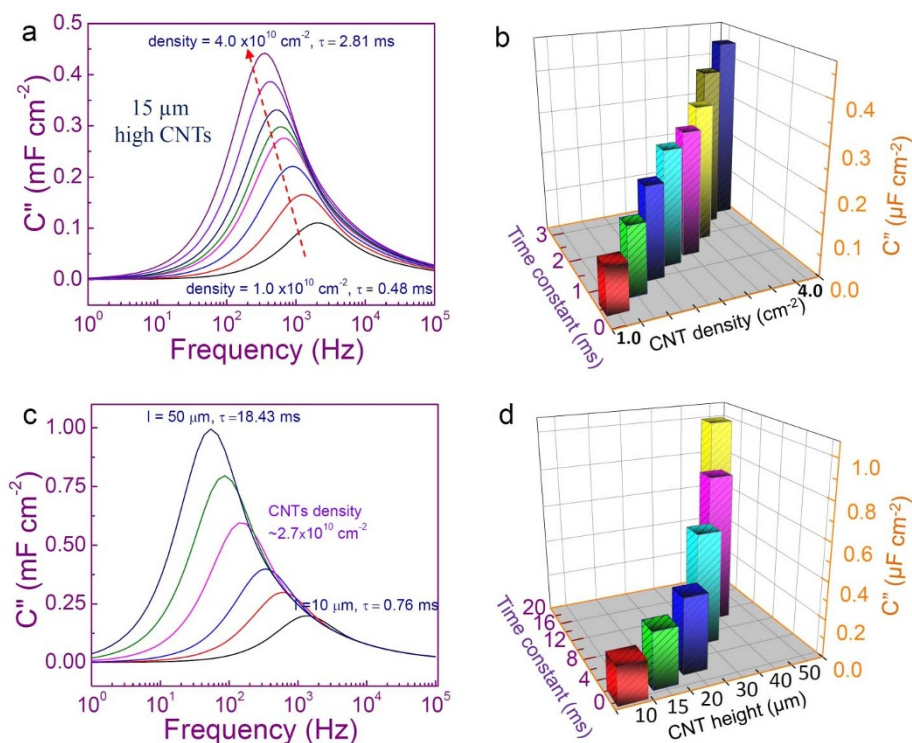


**Figure 4** | (a) Imaginary capacitance in terms of CNT density varying from  $1.0 \times 10^{10}$  to  $4.0 \times 10^{10} \text{ cm}^{-2}$  for a given CNT length of 15  $\mu\text{m}$  and (b) the dependence of capacitance and relaxation time constant on the CNT density. (c) Imaginary capacitance for a height varying from 10 to 50  $\mu\text{m}$  and (d) the dependence of capacitance and relaxation time constant on the CNT height for a given CNT density of  $2.7 \times 10^{10} \text{ cm}^{-2}$ .



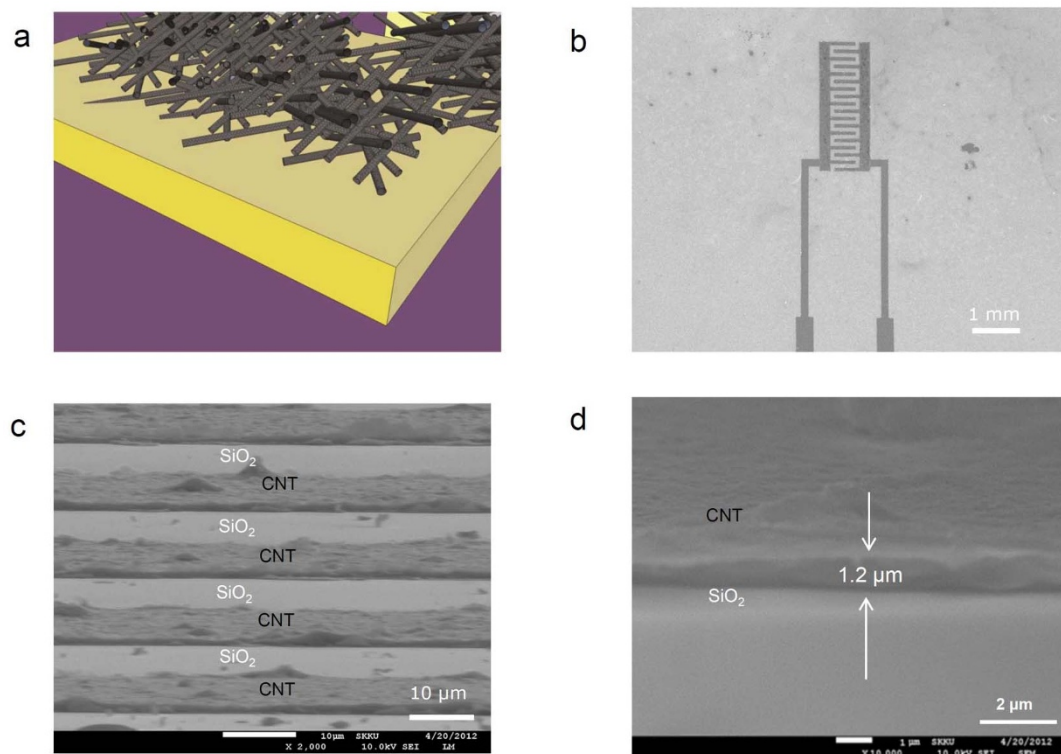


**Figure 5** | (a) Schematic of micro-supercapacitor of spray-deposited re-SWCNT. SEM images of (b) micro-device and (c) magnified micro-electrode. (d) Measurement of a height 1.2  $\mu\text{m}$ .

inter-digital structure. The film thickness of the deposited re-SWCNTs was about 1.2  $\mu\text{m}$ .

The imaginary part of the capacitance from EIS was obtained in a frequency range 1 Hz to 100 kHz to investigate the rate capability of the re-SWCNT based micro-device. The obtained data were compared with v-MWCNT based device with a height of 10  $\mu\text{m}$  for both types of electrolytes of  $\text{Li}_2\text{SO}_4$  (Fig. 6a) and  $\text{LiPF}_6$  (Fig. 6b). The re-SWCNT based device exhibited much slower rate capability with the relaxation time constants of 17.73 ms in  $\text{Li}_2\text{SO}_4$  (Fig. 6a) and

35.96 ms in  $\text{LiPF}_6$  (Fig. 6a) compared to respective values of 0.76 and 2.23 ms for v-MWCNT based devices. The fast rate capability of v-MWCNT device originates clearly from the well aligned mesopores between CNTs such that ion transport can be easily facilitated through pores (Fig. 6c). On the other hand, the re-SWCNTs provide randomly oriented pore distribution which limits ion diffusion through entangled SWCNT network. The total mass of active materials was estimated to be  $\sim 3.0 \mu\text{g}$  for 1.2  $\mu\text{m}$  thick re-SWCNT based device and  $\sim 0.27 \mu\text{g}$  for 10  $\mu\text{m}$  long v-MWCNT based device,

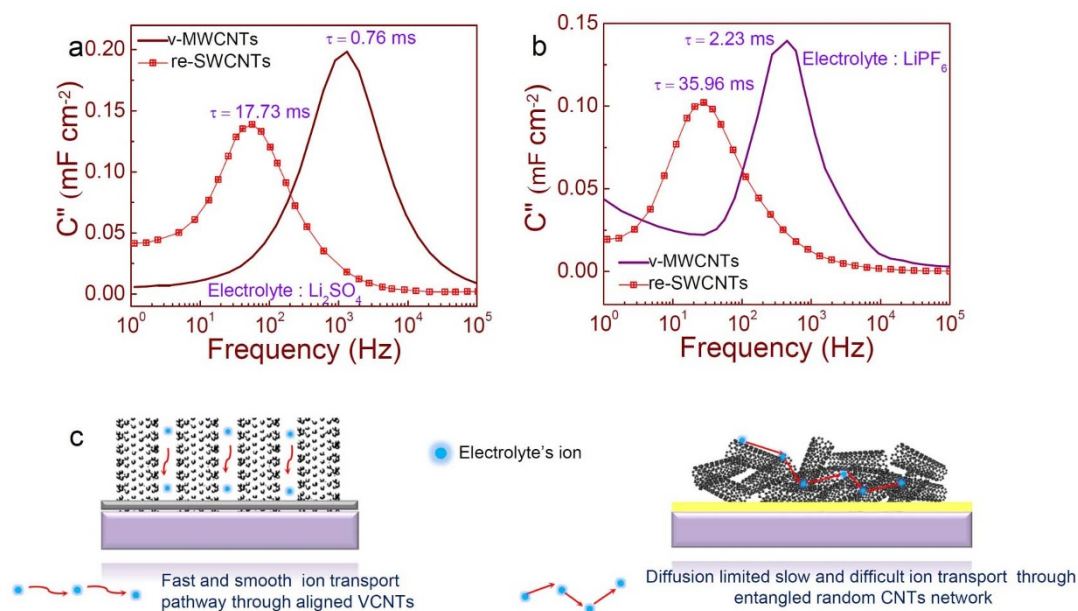


**Figure 6** | Comparative complex capacitance plots for 10  $\mu\text{m}$  long v-MWCNTs and 1.2  $\mu\text{m}$  thick re-SWCNTs in (a)  $\text{Li}_2\text{SO}_4$  and (b)  $\text{LiPF}_6$ . (c) Schematic of ion diffusion through v-MWCNTs and re-SWCNT based micro-devices.



respectively (See S.I. S7). In spite of larger mass for the case of SWCNT based device, larger current was obtained for v-MWCNT based device. SWCNTs were randomly entangled and packed into small volume (1.2  $\mu\text{m}$  thickness), leading to a complicated porous structure which in turn results in extremely difficult ion diffusion, in good contrast with the sparsely spaced v-MWCNTs (10  $\mu\text{m}$  height).

The influence of the difference in the pore distribution for both devices was clearly manifested in the cyclic voltammetry (CV) experiments using  $\text{LiPF}_6$  (Fig. 7). The height of v-MWCNTs was 15  $\mu\text{m}$ , while the thickness of spray deposited randomly entangled CNTs was 1.2  $\mu\text{m}$ . CV curves with an potential window of 0–2.5 V were plotted together for both types of active materials. Initially at lower scan rates (1–10  $\text{Vs}^{-1}$ ) both devices resulted in nearly rectangular shapes of CV curves. On the other hand, with further increase of the scan rates, CV curves of randomly entangled structures were severely distorted. This implies that for v-MWCNTs, ions can access easily to the surface of the active materials even at higher scan rates, whereas re-SWCNT device suffers from slow ion diffusion by the limited accessibility of entangled SWCNT network. Note that at a scan rate of 1000  $\text{Vs}^{-1}$  the current was not even measurable in re-SWCNT device. On the other hand, the ultrafast scan rates for

v-MWCNT device were observed where the current increased linearly up to 600  $\text{Vs}^{-1}$ . Yet both devices showed excellent rate capability compared to conventional supercapacitors<sup>14</sup>. Nearly rectangular CV curves confirmed the formation of efficient electric double layer capacitance and very fast charge transfer within electrodes. The aligned structure outperformed the entangled random structure in term of perfect electric double layer formation and high power capability (rate capability). To our surprise, even at an extremely high scan rate of 1000  $\text{Vs}^{-1}$ , the shape of CV curve for v-MWCNTs was still retained, which is to our knowledge an unprecedented performance for any kind of supercapacitor developed so far. The current density which is normalized by the total area of both electrodes was plotted as a function of the scan rate for both devices in Fig. 7g. The linear current response with increasing scan rate is an indication of high rate capability of v-MWCNT capacitor. The v-MWCNT capacitor exhibited an outstanding performance of linear current response up to an extremely high scan rate of 600  $\text{Vs}^{-1}$ , still maintaining high current even at 1000  $\text{Vs}^{-1}$ . On the other hand, the current response of re-SWCNT capacitor was linear up to the scan rate of 20  $\text{Vs}^{-1}$  and saturated at a scan rate of 100  $\text{Vs}^{-1}$ , in good contrast with that of v-MWCNT device.

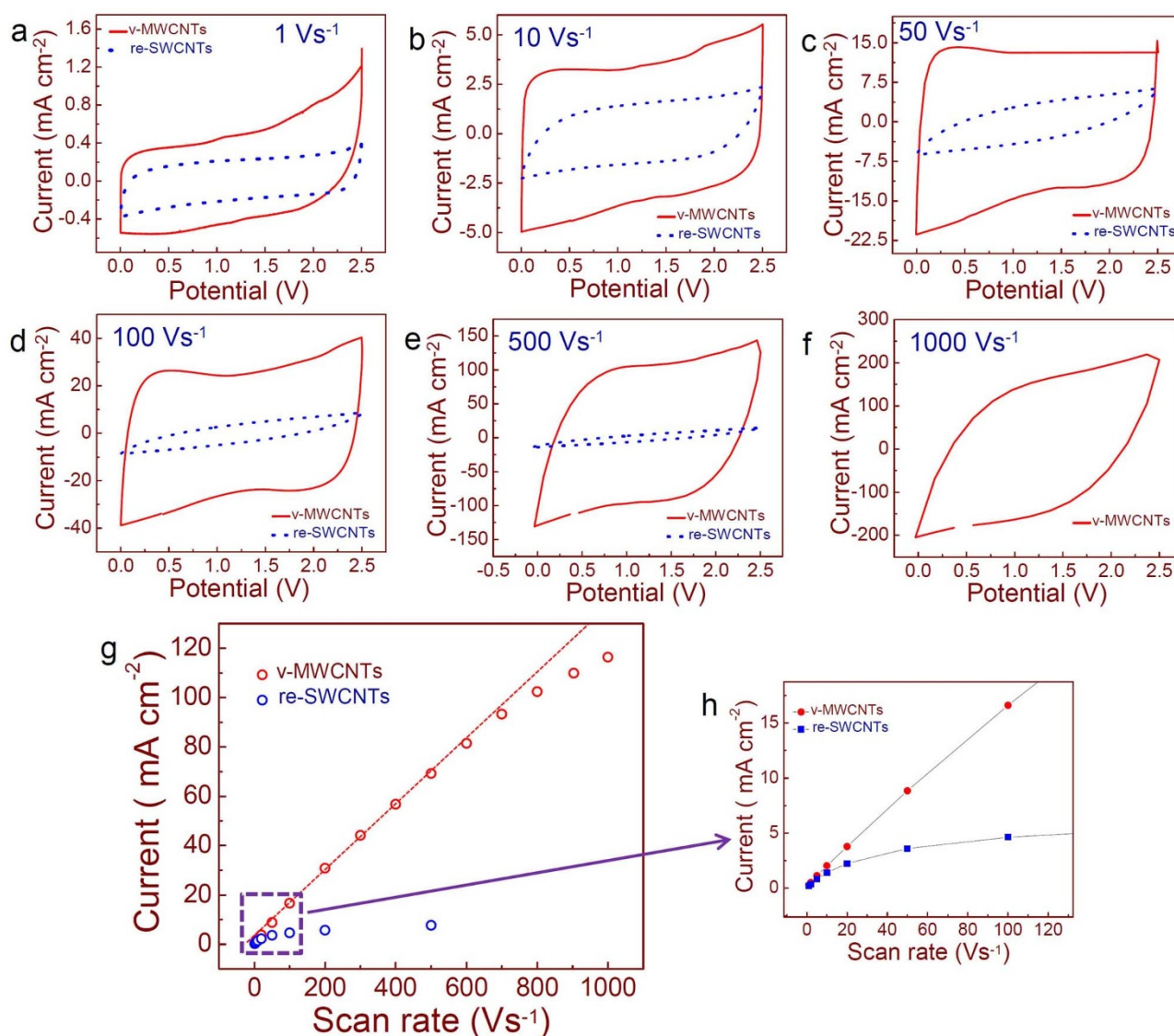


**Figure 7** | (a–e) A comparative ultra-high scan rate performance in  $\text{LiPF}_6$  for 10  $\mu\text{m}$  long v-MWCNT and 1.2  $\mu\text{m}$  thick re-SWCNT based micro-device. (f) v-MWCNT based device at a scan rate of 1000  $\text{Vs}^{-1}$ . (g) Comparison of current densities as a function of scan rate and (h) expanded region at low scan rate.



Rate capability was again investigated in aqueous electrolyte (1 M  $\text{Li}_2\text{SO}_4$ ), CV was conducted for both types of devices and the obtained performance was superior in comparison with those with  $\text{LiPF}_6$  in terms of rate capability (S.I. Fig. S6). In  $\text{Li}_2\text{SO}_4$ , v-MWCNTs showed a linear current response up to a scan rate of  $800 \text{ Vs}^{-1}$  compared to that of  $600 \text{ Vs}^{-1}$  in  $\text{LiPF}_6$ . Shapes of CV curves were also nearly close to be rectangular compared to that of  $\text{LiPF}_6$ . This behavior of better rate capability in aqueous electrolyte can be explained by higher conductivity and smaller ion sizes of aqueous electrolyte than those of organic electrolyte<sup>12</sup>. The v-MWCNTs outperformed re-SWCNTs in aqueous electrolyte ( $\text{Li}_2\text{SO}_4$ ) (S.I. Fig. S6). In order to understand the effect of electrolyte, ion size, and conductivity, we presented the current density comparison in two different types of electrolytes for both types of devices based on v-MWCNTs and re-SWCNTs (Fig. S7a, S7b). Aqueous electrolyte clearly revealed the better performance than organic electrolyte, which can be attributed to higher conductivity of aqueous electrolyte and its smaller ion sizes.

Energy storage performances of these two different porous structures are shown in Ragone plot in Fig. 8 (See also S.I. S4). The v-MWCNT based device exhibited an energy density of  $22 \text{ Wh kg}^{-1}$  at an average power density of  $1560 \text{ W kg}^{-1}$ . The average power density was increased up to an extremely high value of  $1.39 \times 10^7 \text{ W kg}^{-1}$ , while still retaining an energy density of  $\sim 6.45 \text{ Wh kg}^{-1}$ . The v-MWCNT based micro-supercapacitor show much better energy and power density than re-SWCNT based device. This is a direct consequence of high rate capability of the device. The device performance was again compared in terms of apparent volumetric energy and power density (Fig. 8b and see S.I. S5). Although the power performance of v-MWCNT based micro-device was excellent in terms of apparent power density, the energy density was low, reaching  $\sim 30\%$  lower than that of our re-SWCNT based device. This comparatively small value of the energy density of the v-MWCNT based device can be attributed to comparatively low CNT mass per unit electrode area. The micro-device based on the v-MWCNT structure with a CNT density of  $2.7 \times 10^{10} \text{ cm}^{-2}$ , has  $\sim 95\%$  porosity (See S.I. S6). Therefore, if the density of the v-MWCNT array increases, the

total mass of CNTs per unit area will increase and hence the apparent volumetric energy density will increase.

Yet, there will be a trade-off between energy density and the rate capability. Therefore, in order to investigate in more detail, we obtained a simulated Ragone plot for different CNT densities. Higher CNT density gives higher energy density (Fig. 8c). The energy density rapidly decreases at low CNT density of  $5 \times 10^9 \text{ cm}^{-2}$ , suggesting that the CNT density is the energy density limiting factor. Figure 8d shows the similar dependence on the CNT length. In this case, energy density decreases linearly as the power density increases. One can optimize the micro-capacitor with various ranges of energy and power density for technological demands which can be obtained without obvious limiting factors.

## Discussion

The model successfully explains how height, pore length, pore radii and electrolyte conductivity of active materials can affect performance of different micro-supercapacitors. Mutual dependence of rate capability and energy storage capacity of a MEMS supercapacitor has been systematically investigated by our TLM-PSD model and relevant experimental studies. Even though a MEMS supercapacitor based on v-MWCNTs has been successfully developed exhibiting an extremely low relaxation time constant of  $0.76 \text{ ms}$ , i.e., with the capability of discharging  $50\%$  of its stored energy in less than  $0.76 \text{ ms}$ , however, the rate capability becomes poor with increasing height and density of active material in v-MWCNTs. The height dependence is also observed for a three dimensional graphene – carbon nanotube carpet supercapacitor<sup>42</sup>. This behavior is successfully explained by our model of the porous structure. Even though longer and denser v-MWCNTs array results in the increased areal and volumetric energy density, some degree of the degradation of the rate capability is unavoidable. This trade-off between energy and power density can be successfully explained in the light of effective pore formation by our model. The longer v-MWCNTs result in longer pore formation, and hence ions suffer larger diffusion resistance through the interstitial pores. This causes slow electrochemical response, and hence higher value of relaxation time constant is

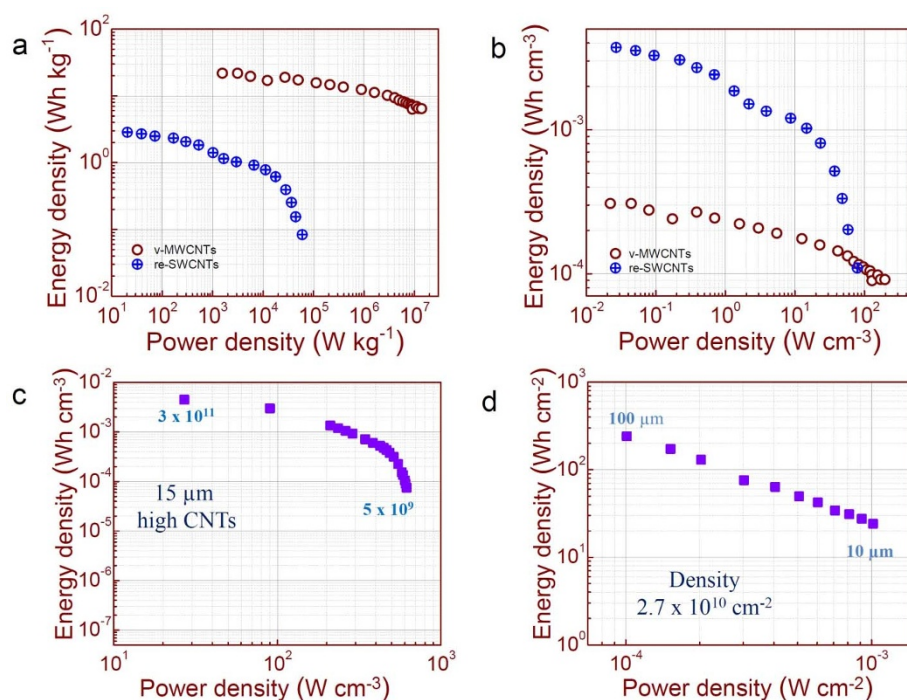


**Figure 8** | (a) Gravimetric and (b) volumetric Ragone plots for v-MWCNT and re-SWCNT based micro-devices. Simulation results of Ragone plots in terms of v-MWCNT density at a given CNT height of  $15 \mu\text{m}$  (c) and height at a given CNT density of  $2.7 \times 10^{10} \text{ cm}^{-2}$  (d).





predicted. Pore radii depend on the densities of v-MWCNT arrays. Higher CNT density results in formation of pores with smaller radii, which again affects ion diffusion by increasing effective pore resistance. From our proof of concept experiment, the aligned porous structure outperforms re-SWCNT based device in terms of rate capability. This result can be realized in light of pore size distribution of the active materials. The v-MWCNTs creates an aligned porous structure which is mainly mesoporous compared to that of re-SWCNTs in which a majority of surface area is contributed from micropores.

Situation becomes even worse, when pore sizes are comparable to ion sizes. This leads to extremely slow ion diffusion inside pores during adsorption process, and similarly very slow desorption during discharge process can be observed. These slow adsorption–desorption processes eventually delay the response of a capacitor to any electric field change. Therefore, bundle formation in re-SWCNTs structure results in high value of relaxation time constant. The response becomes even slower when electron transportation within the electrode material suffers from poor conductivity of the material. Randomly distributed SWCNT junctions provide high resistances and thus electron transport becomes difficult within the active material, where in the contrary vertically aligned structure provides excellent electron transport pathway. Figure 6c schematically represents fast and smooth ion transport through the interstitial mesopores of vertically aligned CNTs, in contrast to the diffusion limited slow ion transport through randomly entangled CNTs.

On the other hand, the model is based on uniform interstitial mesoporous distribution of v-MWCNTs, and microporous contributions from different defects are not included, although this can be in principle implemented by introducing an appropriate mathematical pore size distribution function in equation (2). Based on our simulation results and in the light of above comparative discussion between aligned and randomly entangled structure, it can be realized that how different porous structures with different pore radii and pore lengths, and different nature of pore distribution of active material can greatly influence the rate capability of a micro-supercapacitor which results in different values of relaxation time constants for different active materials and electrolytes (as listed in S.I. Table – S2).

In our model, we did not model theoretically the re-SWCNT based device as it is extremely difficult to obtain a suitable pore size distribution for a complete random distribution, contrary to an aligned and regular porous structure. Nevertheless, from extensive theoretical analyses and related experimental studies, a basic design rule for a supercapacitor can be realized. Based on the analyses of this model, it is possible to theoretically predict change in relaxation time constant (or characteristic frequency position) as a function of electrolyte conductivity and size of pores. Therefore, it is possible to extract useful information prior to any device fabrication. With given information on pore size distribution of the active material, energy density and power density of the device can be tuned and a desirable rate capability can be obtained. We believe that our simple model of explaining dynamical behavior will be used to predict and design numerous types of practical supercapacitors and micro-supercapacitors.

## Methods

**Fabrication of v-MWCNT based micro-supercapacitor.** The v-MWCNTs were directly grown on the electrode of the micro-supercapacitor device using an atmospheric pressure thermal chemical vapor deposition (APCVD) chamber. CNTs were grown from 1 nm thick iron (Fe) catalyst layer, deposited on a patterned 20 nm thick aluminum (Al) layer. The first step of fabrication was patterning of 100 nm thick Gold (Au) contact pads on a SiO<sub>2</sub> wafer (300 nm thick oxide layers) to make contact electrodes by conventional photolithography and evaporation techniques. The Au layer was deposited by thermal evaporation technique, following an e-beam evaporation of 5 nm thick Cr layer on SiO<sub>2</sub> wafer. Cr layer was needed to enhance the adhesion between Au layer and SiO<sub>2</sub> wafer. SiO<sub>2</sub> wafer worked as an insulating region, separating interdigital electrodes. After that, 20 nm thick Al layer was patterned by thermal evaporator as inter-digital fingers and connected to the Au contact electrodes. Finally 1 nm thick Fe catalyst layer was deposited on Al layer by e-beam

deposition technique. Deposition rate was kept at 0.2 Å s<sup>-1</sup> and 0.1 Å s<sup>-1</sup> for Al layer and Fe layer respectively, which was optimized for best growth condition in our previous work<sup>45</sup>. The device had then been loaded inside the atmospheric pressure thermal chemical vapor deposition (APCVD) chamber. Temperature was increased to 750 °C over 10 min in the presence of Ar gas. A mixture of Ar, ethylene (C<sub>2</sub>H<sub>4</sub>), and hydrogen (H<sub>2</sub>) gases with corresponding flow rates of 300, 110, and 500 standard cubic centimeters per minute (sccm), was introduced inside the chamber for growth of the v-MWCNTs. We varied v-MWCNT growth time for different micro-devices, and obtained different height of the grown v-MWCNTs as 10 μm, 15 μm, and 50 μm, respectively.

**Fabrication of re-SWCNTs based micro-supercapacitor.** For re-CNTs based device, Au layer (100 nm) was used for both supporting and contact electrodes. HiPco SWCNTs (Unidym Inc.) were dispersed in dichloroethane (DCE) solution to use as an active material for the supercapacitor device. Then the dispersed SWCNTs were spray-deposited selectively only on the patterned electrode regions on top of Au electrodes. Finally the electrodes were dried completely, and the micro-device was ready to use.

**Electrochemical characterization.** The micro-devices were electrochemically characterized by cyclic voltammetry (CV) measurements, using 1.15 M LiPF<sub>6</sub> in EC/DEC solvent [EC/DEC = 3/7 (v/v)] and a potential window of 0–2.5 V was achieved. Also 1 M Li<sub>2</sub>SO<sub>4</sub> was used for CV measurement in aqueous electrolyte. A Biologic VMP3 machine was used for these measurements.

**Morphological characterization.** Scanning electron microscopy (SEM) images were obtained using a JEOL JSM7000F.

- Chimola, J., Yushin, G., Dash, R. & Gogosti, Y. Effect of pore size and surface area of carbide derived carbons on specific capacitance. *J. Power Sources* **158**, 765–772 (2006).
- Chimola, J. *et al.* Anomalous increase in carbon capacitance at pore sizes less than 1 nanometer. *Science* **313**, 1760–1763 (2006).
- Simon, P. & Gogosti, Y. Materials for electrochemical capacitors. *Nat. Mater.* **7**, 845–854 (2008).
- Liu, C., Li, F., Ma, L.-P. & Cheng, H.-M. Advanced materials for energy storage. *Adv. Mater.* **22**, E28–62 (2010).
- Frackowiak, E. Carbon materials for supercapacitor application. *Phys. Chem. Chem. Phys.* **9**, 1774–85 (2007).
- Chaikittisilp, W., Ariga, K. & Yamauchi, Y. A new family of carbon materials: synthesis of MOF derived nanoporous carbons and their promising applications. *J. Mater. Chem. A* **1**, 14–19 (2013).
- Radhakrishnan, L. *et al.* Preparation of microporous carbon fibers through carbonization of Al-based porous coordination polymer (Al-PCP) with furfuryl alcohol. *Chem. Mater.* **23**, 1225–1231 (2011).
- Chaikittisilp, W. *et al.* Nanoporous carbons through direct carbonization of a zeolitic imidazolate framework for supercapacitor electrodes. *Chem. Commun.* **48**, 7259–7261 (2012).
- Hu, M. *et al.* Direct carbonization of Al-based porous coordination polymer for synthesis of nanoporous carbon. *J. Am. Chem. Soc.* **134**, 2864–2867 (2012).
- Ghosh, A. & Lee, Y. H. Carbon-based electrochemical capacitors. *ChemSusChem* **5**, 480–99 (2012).
- Ghosh, A. *et al.* High pseudocapacitance from ultrathin V<sub>2</sub>O<sub>5</sub> films electrodeposited on self-standing carbon-nanofiber paper. *Adv. Funct. Mater.* **21**, 2541–2547 (2011).
- Lokhande, C. D., Dubal, D. P. & Joo, O.-S. Metal oxide thin film based supercapacitors. *Curr. Appl. Phys.* **11**, 255–270 (2011).
- Wang, K. *et al.* An all-solid-state flexible micro-supercapacitor on a Chip. *Adv. Energy Mater.* **1**, 1068–1072 (2011).
- Beidaghi, M. & Wang, C. Micro-supercapacitors based on three dimensional interdigital polypyrrole/C-MEMS electrodes. *Electrochim. Acta* **56**, 9508–9514 (2011).
- Sun, W. & Chen, X. Preparation and characterization of polypyrrole films for three-dimensional micro supercapacitor. *J. Power Sources* **193**, 924–929 (2009).
- Sun, W. & Chen, X. Fabrication and tests of a novel three dimensional micro supercapacitor. *Microelectron. Eng.* **86**, 1307–1310 (2009).
- Sun, W., Zheng, R. & Chen, X. Symmetric redox supercapacitor based on micro-fabrication with three-dimensional polypyrrole electrodes. *J. Power Sources* **195**, 7120–7125 (2010).
- Pech, D. *et al.* Elaboration of a microstructured inkjet-printed carbon electrochemical capacitor. *J. Power Sources* **195**, 1266–1269 (2010).
- Chmiola, J., Largeot, C., Taberna, P.-L., Simon, P. & Gogosti, Y. Monolithic carbide-derived carbon films for micro-supercapacitors. *Science* **328**, 480–483 (2010).
- Gao, W. *et al.* Direct laser writing of micro-supercapacitors on hydrated graphite oxide films. *Nat. Nanotechnol.* **6**, 496–500 (2011).
- Beidaghi, M. & Wang, C. Micro-supercapacitors based on interdigital electrodes of reduced graphene oxide and carbon nanotube composites with ultrahigh power handling performance. *Adv. Funct. Mater.* **22**, 4501–4510 (2012).
- Pech, D. *et al.* Ultrahigh-power micrometre-sized supercapacitors based on onion-like carbon. *Nat. Nanotechnol.* **5**, 651–4 (2010).



23. El-Kady, M. F. & Kaner, R. B. Scalable fabrication of high-power graphene micro-supercapacitors for flexible and on-chip energy storage. *Nat. Commun.* **4**, 1475 (2013).
24. Miller, J. R., Outlaw, R. & Holloway, B. C. Graphene double-layer capacitor with ac line-filtering performance. *Science* **329**, 1637–9 (2010).
25. Sheng, K., Sun, Y., Li, C., Yuan, W. & Shi, G. Ultrahigh-rate supercapacitors based on electrochemically reduced graphene oxide for ac line-filtering. *Sci. Rep.* **2**, 247 (2012).
26. De Levie, R. Electrochemical response of porous and rough electrodes. *Adv. Electroch. El. Eng.* **6**, 329–397 (1967).
27. De Levie, R. On porous electrodes in electrolyte solutions. *Electrochim. Acta* **8**, 751–780 (1963).
28. De Levie, R. On porous electrodes in electrolyte solutions-IV. *Electrochim. Acta* **9**, 1231–1245 (1964).
29. Song, H., Jung, Y., Lee, K. & Dao, L. H. Electrochemical impedance spectroscopy of porous electrodes: the effect of pore size distribution. *Electrochim. Acta* **44**, 3513–3519 (1999).
30. Futaba, D. N. *et al.* Shape-engineerable and highly densely packed single-walled carbon nanotubes and their application as super-capacitor electrodes. *Nat. Mater.* **5**, 987–94 (2006).
31. Beguin, F. & Frackowiak, E. *Carbons for Electrochemical Energy Storage and Conversion Systems*. (CRC Press, Taylor & Francis Group 2010).
32. Taberna, P. L., Simon, P. & Fauvarque, J. F. Electrochemical characteristics and impedance spectroscopy studies of carbon-carbon supercapacitors. *J. Electrochem. Soc.* **150**, A292 (2003).
33. Luo, J.-Y., Zhou, D.-D., Liu, J.-L. & Xia, Y.-Y. Hybrid aqueous energy storage cells using activated carbon and lithium-ion intercalated compounds IV. Possibility of using polymer gel electrolyte. *J. Electrochem. Soc.* **155**, A789–A793 (2008).
34. Signorelli, B. R., Ku, D. C., Kassakian, J. G. & Schindall, J. E. Electrochemical double-layer capacitors using carbon nanotube electrode structures. *Proc. IEEE* **97**, 1837–1847 (2009).
35. Chen, P. *et al.* Preparation and characterization of flexible asymmetric supercapacitors based on transition-metal-oxide nanowire/single-walled carbon nanotube hybrid thin-film electrodes. *ACS Nano* **4**, 4403–4411 (2010).
36. Conway, B. E. *Electrochemical Supercapacitors: Scientific Fundamentals and Technological Applications*. (Kluwer Academic Press/Plenum Publishers, New York, NY, 1999).
37. Feng, G. *et al.* The importance of ion size and electrode curvature on electrical double layers in ionic liquids. *Phys. Chem. Chem. Phys.* **13**, 1152–61 (2011).
38. Kielland, J. Individual Activity Coefficient of ions in aqueous solutions. *J. Am. Chem. Soc.* **59**, 1675–1678 (1937).
39. Pujari, B. R., Barik, B. & Behera, B. Dielectric constants of some miscible aqueous-organic solvent mixtures. *Phys. Chem. Liquids* **36**, 105–112 (2006).
40. Common solvent properties. <http://macro.lsu.edu/HowTo/solvents.htm> (accessed on 20. 05. 2013).
41. Esconjauregui, S. *et al.* Growth of ultrahigh density vertically aligned carbon nanotube forests for interconnects. *ACS Nano* **4**, 7431–6 (2010).
42. Lin, J. *et al.* 3-Dimensional graphene carbon nanotube carpet-based microsupercapacitors with high electrochemical performance. *Nano Lett.* **13**, 72–8 (2013).
43. Lee, I. H. *et al.* Criteria for producing yarns from vertically aligned carbon nanotubes. *Nano* **5**, 31–38 (2010).

## Acknowledgments

This work was supported by the Institute for Basic Science (IBS) in Korea and WCU (World Class University) program through the National Research Foundation of Korea funded by the Ministry of Education (R31-2008-10029).

## Author contributions

A.G. has carried out micro-supercapacitor design and fabrications, electrochemical measurements, data analyses, and simulations for micro-supercapacitor electrodes. A.G. and Y.H.L. have designed the main concept of the work and wrote the manuscript. V.T.L. has grown vertically aligned carbon nanotubes. J.J.B. performed electric field line simulations.

## Additional information

**Supplementary information** accompanies this paper at <http://www.nature.com/scientificreports>

**Competing financial interests:** The authors declare no competing financial interests.

**How to cite this article:** Ghosh, A., Le, V.T., Bae, J.J. & Lee, Y.H. TLM-PSD model for optimization of energy and power density of vertically aligned carbon nanotube supercapacitor. *Sci. Rep.* **3**, 2939; DOI:10.1038/srep02939 (2013).



This work is licensed under a Creative Commons Attribution-NonCommercial-NoDerivs 3.0 Unported license. To view a copy of this license, visit <http://creativecommons.org/licenses/by-nc-nd/3.0>